Crystallization of finite-extensible nonlinear elastic Lennard-Jones coarse-grained polymers

Julien Morthomas, Claudio Fusco, Zengqiang Zhai, Olivier Lame, and Michel Perez
INSA de Lyon, Université de Lyon, MATEIS, UMR CNRS 5510, 69621 Villeurbanne, France
(Received 10 July 2017; published 27 November 2017)

The ability of a simple coarse-grained finite-extensible nonlinear elastic (FENE) Lennard-Jones (LJ) polymer model to be crystallized is investigated by molecular dynamics simulations. The optimal FENE Lennard-Jones parameter combinations (ratio between FENE and LJ equilibrium distances) and the optimal lattice parameters are calculated for five different perfect crystallite structures: simple tetragonal, body-centered tetragonal, body-centered orthorhombic, hexagonal primitive, and hexagonal close packed. It was found that the most energetically favorable structure is the body-centered orthorhombic. Starting with an equilibrated polymer liquid and with the optimal parameters found for the body-centered orthorhombic, an isothermal treatment led to the formation of large lamellar crystallites with a typical chain topology: folded, loop, and tie chains, and with a crystallinity of about 60%–70%, similar to real semicrystalline polymers. This simple coarse-grained Lennard-Jones model provides a qualitative tool to study semicrystalline microstructures for polymers.

DOI: 10.1103/PhysRevE.96.052502

I. INTRODUCTION

The mechanical properties of semicrystalline polymers result from their multiscale complex microstructure, mainly characterized by stacking of crystalline and amorphous lamellae of a few microns length and a few nanometers thickness [1–6]. Several unknown features are resistant to experimental analysis mainly because of the nanometric scale. For instance, interphase layers, but especially specific molecules such as tie molecules (TMs), which link two adjacent crystallites, are known to play an important role in the mechanical properties even if no quantitative description of their contribution on the mechanical properties is available [7]. Indeed, no experimental technique permits to investigate the concentration and topology of TMs. The TM content is therefore evaluated only indirectly by mechanical testing or by statistical analysis [8–11].

Molecular dynamics (MD) simulations, which can benefit from increasing computing power, are excellent tools to overcome the difficulties of experimental measurements and can be used to study the nonequilibrium process of crystallization at the nanoscale and the mechanical properties of nanostructured systems, which are important in particular for polymers [12–64]. MD simulations of semicrystalline polymers can be performed at different length and time scales with different levels of complexity. Explicit atom (EA) models, where all the hydrogen atoms are taken into account explicitly, can give precious insight on the role of TMs on the mechanical properties of semicrystal [18,19] but they are time consuming since they treat explicitly C-H bond vibrations: Since the equilibration time is thus very large for system sizes of interest they are not suited for studying large deformations. In order to decrease computational time, an alternative approach is to consider each unit or "bead" of the polymer chain either as a CH_2 or CH_3 group (united atom (UA) models [20–47]), or as a few structural carbons or monomers (coarse-grained (CG) models [48–55,57–60]). Order-oriented phase structure was observed and discussed with UA models mimicking *n*-alkane or polyethylene polymer for a single chain [21–25] and for multiple length chains in vacuum [24,26–30]. The chain folding phenomenon with various chain lengths and torsional angle deformation barriers has been examined [22,23]. UA Langevin dynamics simulations have been performed to understand early-stage polymer crystallization [24,25], the diffusion of chains to the crystal growth front [25,26], and crystallization in extensional flow [27]. Nucleation processes and crystal growth from an isotropic melt [31–33], along substrates [32,34–39] or from an oriented melt [40–45], and cold crystallization after a rapid quenching of a melt [37,46] have also been studied with UA models. Unfortunately, the computational time to study crystallization would not be sufficient to simulate the growth of large lamellae. In CG models the size of the system as well as the time scale involved are large enough to fully address the problems of the size, thickness, and shape of the lamellae as well as the molecular topology (e.g., TM concentration). Moreover, the mechanical properties can be easily evaluated even for large deformation [13–17]. In CG models, bonded units in a chain interact through springs. The stiffness of the chain can be modeled by bending and/or torsional potentials, while nonconnected units interact through a Lennard-Jones potential including excluded volume and van der Waals interactions. In these models, it is possible to optimize the potential parameters to quantitatively study the crystallization process of specific systems. For example, a CG potential optimized for describing polyvinyl alcohol (CG-PVA) [51] showed realistic chain folded lamellae in semicrystal after rapid quenching [52,53]. In this CG-PVA model only the repulsive part of the Lennard-Jones potential is taken, while the attractive part is replaced by applying an external pressure. This CG-PVA has been used recently to generate semicrystalline systems exhibiting large fraction and density of crystallites and has been proved to successfully mimic the main features of classical semicrystalline systems [16,17]. With the same CG-PVA model, homogeneous nucleation and growth of a single polymer lamellae crystal was observed from a melt via self-seeding [54]. The same authors showed the importance of the entanglement for the crystallization process for nonconfined [55] and confined polymer melts [56]. The minimal approach of the CG model is the qualitative and not quantitative Kremer-Grest (KG) bead-spring model [48] where bonded chain units are connected by finite-extensible nonlinear elastic (FENE) bonds that prevents chain crossing and nonbonded chain units by classical Lennard-Jones potential. Even if the KG model has proved its performance to reproduce

the qualitative behavior of glass polymer [12–15,65,66], as it is, it is not usable to study polymer crystallization with MD. A first solution was to enforce the equilibrium length of bonded units to be commensurate with the equilibrium length of nonbonded units [57]. Massive crystallization was observed, but chain morphology is not realistic and system crystallizes just like a Lennard-Jones liquid. An angular potential to get more realistic crystallites was therefore added [58], but it was limited to relatively small box size.

In this paper, we test the ability of a simple coarse-grained FENE Lennard-Jones potentials model based on the KG model to qualitatively represent all microstructural features exhibited by a real semicrystalline polymer: (i) chains are parallel in the crystal; (ii) the lattice is never cubic due to the strong difference between the C-C bond length and the weak bond length; (iii) crystallites mainly grow perpendicular to the chain direction, thus forming platelike lamellae; (iv) chains are partially folded in a single crystallite; (v) we expect several topologies for the amorphous phase: loop, folded, and pending chains and some chains belong to several crystallites forming TM; (vi) crystallinity degree of linear polymer ranges between 20% and 80%. Even if the KG approach cannot be directly compared to real polymers in a quantitative way, this kind of tool is essentially useful to understand the general features of crystallization in semicrystalline polymers and to test the realism of alternative ideas and concepts that could be then used for modeling of real polymers.

We can use two main numerical strategies to investigate the mechanical behavior of nanostructured systems, such as semicrystalline polymers. The first approach consists in artificially organizing macromolecules into lamellar microstructure as observed for real polymers [18,19,61–64]. This microstructure is realistic and the influence of parameters such as lamellae thicknesses or TM concentrations on the mechanical properties can then be tested in realistic conditions. However, such well-organized microstructures may not be the natural equilibrium for the chosen model system. This is particularly critical when strongly stretching this system, which could lead to a nonrealistic microstructure yielding questionable conclusions on the TM, loop concentration, and thus the deformation mechanisms. The second approach to be used in this paper consists in first equilibrating macromolecules in the melt state and, then, cooling down the system to obtain crystallites [16,17,31,32,52–55,57,58]. Here, the final system is clearly closer to the natural equilibrium of such systems but the resulting microstructures could be far from the experimental observations. Indeed, cooling rates are generally rather high and correspond to extreme quenches, leading to disordered microstructures.

The paper is organized as follows. Section II presents our model, potentials, systems, and computational methods. At the beginning, we will consider perfect crystalline structures with fixed lattice parameters in order to find optimum values of the parameters of the interatomic potential; these structures are then allowed to relax without constraints on the lattice parameters in the following full CG MD simulations to study the crystallization dynamics. In Sec. III, we investigate and select optimal Lennard-Jones lattice parameters obtained from the analysis of Sec. II for five different perfect crystallite structures. This section is also devoted to the thermal stability of selected structures and focuses on natural crystallization from a polymer melt. A conclusion is given in Sec. IV.

II. MODELS AND METHODS

We use a coarse-grained polymer model based on the KG model [48] where polymer chains consist of "beads" representing a few structural units. All simulations are made in three dimensions.

A. Interaction potentials

The model is based on two potentials, where energy, length, and time units are given by ϵ_u, σ_u, and τ_u, respectively (with $\tau_u = \sqrt{m_u \sigma_u^2/\epsilon_u}$, where m_u is the mass unit). The temperature unit is given by ϵ_u/k_B. Intrachain interactions of bonded beads corresponding to covalent bonds are given by a FENE potential:

$$V_{\mathrm{FENE}}(r) = -0.5kR_0^2 \ln\left[1-\left(\frac{r}{R_0}\right)^2\right] + 4\epsilon\left[\left(\frac{\sigma_F}{r}\right)^{12} - \left(\frac{\sigma_F}{r}\right)^{6}\right], \quad (1)$$

with $k = 30\,\epsilon_u/{\sigma_u}^2$, $R_0 = 1.5\,\sigma_u$, $\epsilon = 1\epsilon_u$, and $\sigma_F = 1.05\,\sigma_u$. We choose the value of σ_F such that $V_{\mathrm{FENE}}(r = 1\sigma_u)$ is minimum. All other weak interactions between two beads of different chains or between two nonbonded beads of the same chain are modeled by a simple Lennard-Jones potential:

$$V_{\mathrm{LJ}}(r) = 4\epsilon\left[\left(\frac{\sigma}{r}\right)^{12} - \left(\frac{\sigma}{r}\right)^{6}\right] - 4\epsilon\left[\left(\frac{\sigma}{r_c}\right)^{12} - \left(\frac{\sigma}{r_c}\right)^{6}\right], \quad (2)$$

where $\epsilon = 1\epsilon_u$, $r_c = 2.5\sigma$ is the cutoff radius, and σ is a parameter of the potential that will be adjusted in order to obtain the ideal crystallographic structure of each studied system.

Newton's equations of motion are integrated with the velocity Verlet method with the time step $\Delta t = 0.005\tau_u$.

B. Systems and MD simulation protocol

Real semicrystalline polymers do not exhibit cubic lattice, essentially because the covalent bond length strongly differs from the smaller bond length. In addition, real monomers are never perfectly spherical. Therefore, the lattice with the highest symmetry is orthorhombic (e.g., polyethylene). As a result, the chosen system should not exhibit cubic structure that would authorize unphysical multiple orientation of chains within a crystallite. Here, five lattices are investigated: simple tetragonal (tP), body-centered tetragonal (tI), body-centered orthorhombic (oI), hexagonal primitive (hP), and hexagonal close-packed (hcP). These lattices are presented in Fig. 1. Each lattice is defined by its distance a, b, and c and angle α, β, and γ lattice constants. Nonorthogonal structures (rhombohedral, monoclinic, and triclinic) are not investigated considering that

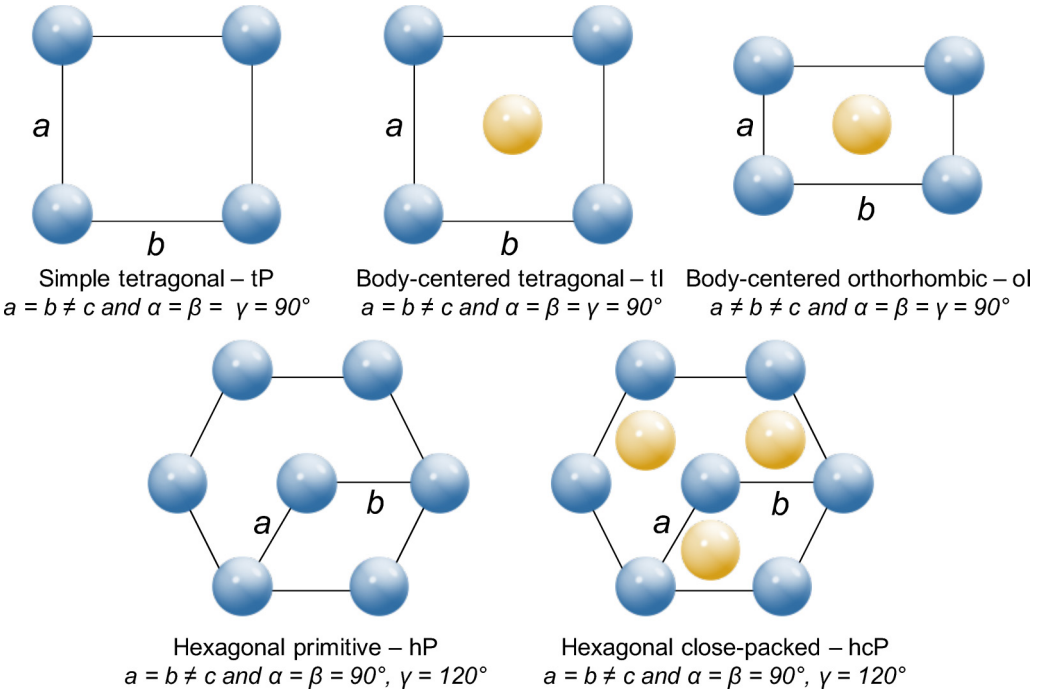

FIG. 1. The top views of simple tetragonal (tP), body-centered tetragonal (tI), body-centered orthorhombic (oI), hexagonal primitive (hP), and hexagonal close-packed (hcP) are represented. The c axis is perpendicular to the paper sheet. The yellow atom at the center of the lattices tI and oI, and the three additional atoms of the lattice hcP compared to hP are in the plane just above or below the reference plane at $\pm c/2$.

the symmetry of the chain is here strong enough to prohibit such lattices.

We perform three kinds of simulations: (i) static ground energy calculations for the above-mentioned perfect crystal structures, first without and after with relaxation and minimization, to optimize σ and the crystallographic parameters of each system; (ii) nonisothermal MD calculations to test the thermodynamic stability of each system; and (iii), isothermal large-scale MD simulations to study crystallization of polymer melts. In simulations (ii) and (iii) no constraints are applied on the lattice parameters of the crystalline structures, which dynamically evolve under the applied force field in the *NPT* ensemble.

1. Statics calculations

Five simulation boxes with fully periodic boundary conditions are made of a periodic arrangement of 1600 straight chains of 20 beads, respectively, with the five lattices presented in Fig. 1, where the chain axis is in the c direction (perpendicular to the paper sheet in Fig. 1). The box size in the c direction corresponds to about three times the maximum cutoff radius r_c. The chain ends are eliminated as the first and last atoms of each chain are bonded by FENE bonds, thanks to the periodic boundary conditions, as if each bead is identical and included in an infinite perfect crystal. As a consequence, no surface energy affects the result.

The aim is to find the best structure to favor crystal stability and further crystallization. Firstly, the energy of the investigated configurations for several values of the potential parameter σ and the crystallographic parameter a/c with $c = 1\sigma_u$ is measured without any modification of the crystal's perfect structure; i.e., no minimization and no relaxation are performed. The σ parameter varies from 0.05 to $2.5\sigma_u$ with the increment $0.01\sigma_u$ and a from 0.5 to $3\sigma_u$ with the increment $0.001\sigma_u$. During this stage, we fix $a = b$ for the tP, tI, hP, and hcP structures, and $b = a\sqrt{3}$ for the oI structure, so that the interchain distance is equal to a. A set of parameters $\sigma_{\min}$ and $a_{\min}/c$ for which the energy is minimized is then found for each structure. Starting from configurations with $a = a_{\min}$, minimization computations by conjugate gradient algorithm at a pressure of $0.0\epsilon_u/\sigma_u^3$ are then performed, for σ varying from $\sigma_{\min} - 0.04$ to $\sigma_{\min} + 0.04$ with the increment $0.001\sigma_u$. These minimization computations allow the relaxation of the box in all directions to find a best set of parameters: σ and the crystallographic parameters a, b, and c. of each system.

2. Melting

In order to study the melting, simulation boxes are made of a periodic arrangement of 1600 straight chains of 100 beads. In order to avoid undesired surface effects[1], the two chain ends are randomly positioned along each straight chain. Thermal stability has been tested along a thermal cycle consisting in a ramp from 0 to $4\epsilon_u/k_B$ (cooling rate: $0.5 \times 10^{-4}\epsilon_u/k_B/\tau_u$). Time integration has been performed in the *NPT* ensemble with a target pressure of $0.0\epsilon_u/\sigma_u^3$.

[1]Systems with "infinite" loop chains aligned in the z direction and looped by the periodic boundary conditions led to unphysical high melting points. Systems with chain ends located in a plane, forming a free surface (grain boundary), led to complex transformations at low temperature involving the free surface itself. These two cases have therefore been discarded in order to simplify the interpretation of the bulk melting.

3. Isothermal crystallization

Much larger systems consisting of 2688 chains of 101 beads have been generated in order to obtain as many crystallites as possible. Starting from an equilibrated melt at $T = 3.3\epsilon_u/k_B$ see Sec. II C), where it was verified that no crystallization occurs, temperature is then decreased to $2.3\epsilon_u/k_B$ (cooling rate: $5 \times 10^{-6}\epsilon_u/k_B/\tau_u$) and maintained during $4.5 \times 10^5\ \tau_u$. This isothermal temperature has been chosen after an extensive test campaign in order to maximize the size of the crystallites; i.e., the driving force for crystallization is moderate at this temperature, leading to a relatively low density of nuclei of large critical size. Moreover, at this temperature, the relatively high mobility induces a fast growth of crystallites.

C. Preparation of the polymer melt

Polymer chains have been generated and equilibrated using the radical-like polymerization (RLP) method [67]. This method starts with a Lennard-Jones bath of N_{mon} monomers, M of them being radicals. At each growth step, each radical connects with a new monomer with a harmonic bond and transfers the radical to the chosen monomer. Between each growth step, the system is equilibrated during $1.5\tau_u$. When a chain reaches the size N its two radicals are deactivated. At the end of the algorithm M chains of N beads are formed. The unused monomers are removed from the simulation. The system is then equilibrated during $5 \times 10^4\tau_u$ at $T = 4\epsilon_u/k_B$ and $P = 0.5\epsilon_u/\sigma_u^3$ in the NPT ensemble. Then, after the idea of [68], $N-1$ beads are inserted within two beads of the initial chains so that we obtain chains of $2N-1$ beads. At that step, the harmonic potential is replaced by a FENE potential with an equilibrium distance of about $1\sigma_u$. The final system consists of M chains of $2N-1$ beads, for which the interchain distance is about $2\sigma_u$ whereas the distance between two beads in a chain is close to $1\sigma_u$. The system is finally equilibrated at $T = 4\epsilon_u/k_B$ for $5 \times 10^4\tau_u$ (see explanations in Sec. III C 1). For the preparation of our polymer melts we have taken $N_{\text{mon}} = 160000$, $M = 2688$, and $N = 51$.

III. RESULTS

A. Ground energy of crystallographic systems

In this section, the different crystallographic structures introduced in Sec. II will be tested and their stability compared.

For all structures, the ground state energy depends on three variables: a, c, and σ. The aim is to find values of a, c, and σ that will minimize the energy of each structure. In a first stage, as the covalent bond is much stiffer than a weak bond, we chose to set $c = 1\sigma_u$, so that the energy depends only on two parameters, a and σ. No minimization and no relaxation are performed at this stage. Note that, in reality, when considering that the distance a is the distance between two chains and c the distance between two carbon atoms in the same chain, experimental values of a/c are much higher than $1\sigma_u$. For example, they are close to $4\sigma_u$ for polyethylene and polyamide.

In Fig. 2 the energy landscape obtained is represented versus the potential parameter σ and the crystallographic parameter a/c for $c = 1\sigma_u$. Here only the oI structure is represented; however, all the structures exhibit nearly the same appearance. The orange plateau corresponds to a diluted medium where

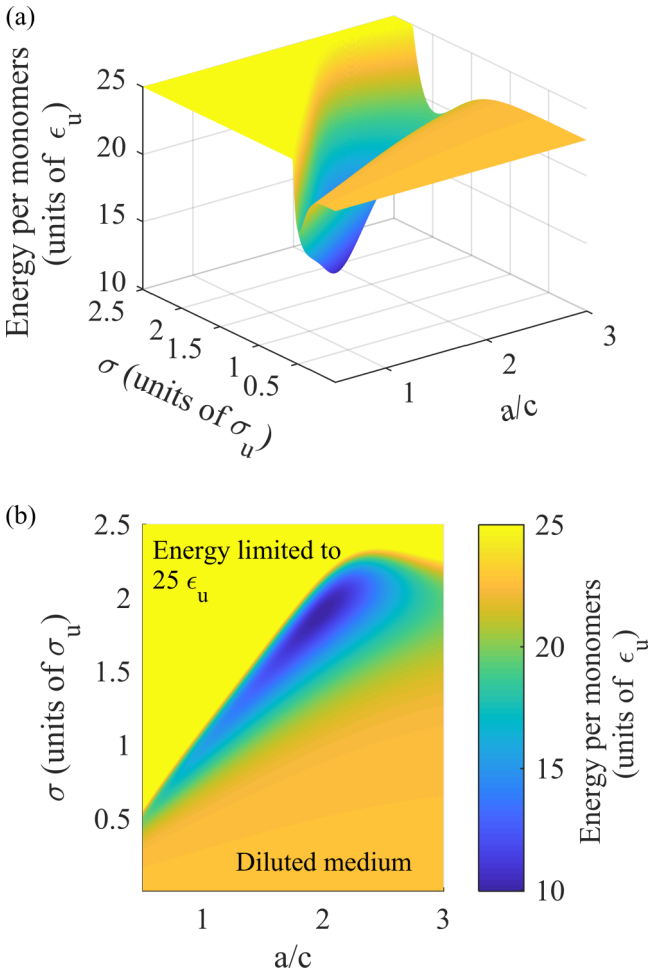

FIG. 2. (a) Side and (b) top view of the energy landscape per monomers versus the potential parameter σ and the crystallographic parameter a/c for body-centered orthorhombic (oI) structure for $c = 1\sigma_u$. For the sake of clarity, high energies are truncated to 25 ϵ_u (top left, yellow region). In this energy landscape a valley appears with an optimum configuration.

chains are far from each other. The value of the energy is essentially given by the FENE contribution. For the sake of clarity, in the yellow region, the energy is arbitrarily truncated to a maximum value of $25\epsilon_u$. Indeed, in this region the chains are close to each other and the Lennard-Jones bonds are in a compressive state increasing the energy strongly. Note that for the very low a/c ratio and high σ the cutoff radius is higher than the box size. However, as these systems are obviously extremely constrained their energies are in any case truncated. Therefore, they are not relevant for the present study. In the energy landscape shown in Fig. 2 a valley appears corresponding to an optimum configuration where most of the atoms are in a position close to their minimal energy. The bottom of this valley is plotted versus σ for all the structures in Fig. 3. In this way, we obtain the set of parameters σ_{min} and a_{min}/c for which the energy of each structure is minimized.

In a second stage, the minimization computation by a conjugate gradient algorithm at a pressure of $0.0\epsilon_u/\sigma_u^3$ is performed allowing the relaxation of the box in all directions. Finally, a minimal relaxed energy configuration is found with

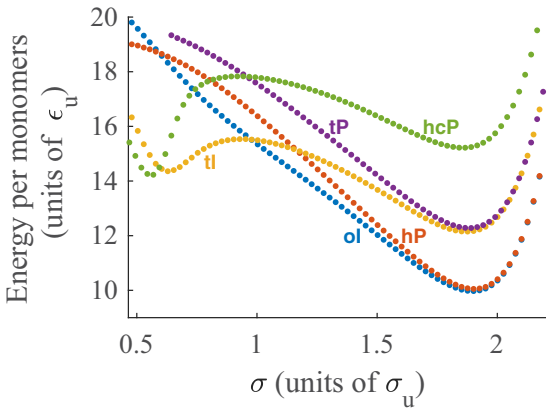

FIG. 3. Bottom of the energy valleys versus the potential parameter σ for all the structures.

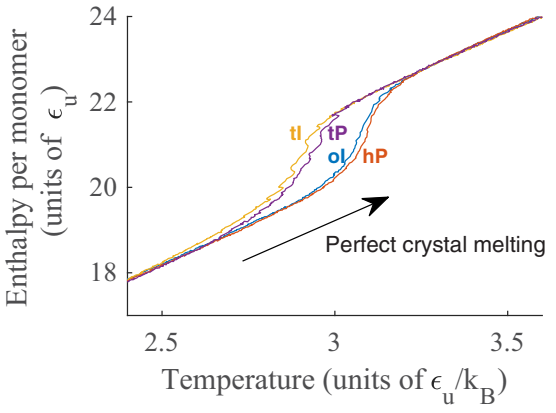

FIG. 4. Thermogram starting from perfect crystal for tP, tI, oI, and hP structures. Only the enthalpy for the temperature ranging from $T = 2.5$ to $4\epsilon_u/k_B$ is plotted.

an optimum set of parameters a, c, and σ; see Table I. Note that after the minimization, the crystallographic configuration of each structure does not change.

It appears that hexagonal primitive (hP) and body-centered orthorhombic (oI) structures exhibit the most stable states for a σ close to $1.89\sigma_u$ and aspect ratio a/c of about 2. The other orthorhombic systems seem to be less stable and the hexagonal compact one is clearly the less stable and is eliminated from the present study. From these first evaluations, only four structures have been selected: tP, tI, oI, and hP.

In the following, structures associated with their optimized σ parameter will be referred to as systems.

B. Melting

Thermal stability of the four different selected systems, oI, tI, tP, and hP, has been tested along a thermal cycle consisting in a ramp from 0 to $4\epsilon_u/k_B$. Figure 4 shows the evolution of the enthalpy of the four investigated systems. It can be noticed that the slope of $H(T)$ versus T is close to 3, which agrees with the equipartition theorem ($\Delta E_k = \Delta E_p = 3/2\ k_B T$) considering three degrees of freedom and negligible pressure ($\Delta H = \Delta E_p + \Delta E_k + \Delta\ (PV)\ \approx 2\Delta E_k = 3k_B T$). For all systems, the enthalpy variation due to melting is approximately $2\epsilon_u$ per atom, which corresponds roughly to $0.15 - 0.20\epsilon_u$ per bond (as in the crystal a bead has approximately ten neighbors when excluding their first intrachain neighbors). At the melting temperature, the total variation of enthalpy $\Delta H = H(T) - H(T = 0)$ is close to $1\epsilon_u$ per bond.

Surprisingly, the enthalpy before melting of the four systems is identical. A closer investigation of the systems' behavior at low temperature shows that less stable systems (tP and tI) transform into more stable structures closer to hP or oI. This can be understood noticing that all σ parameters are very close (see Table I) whereas the energy of the oI and hP structure is much more favorable, even for the σ parameters optimized for tI and tP structures.

The melting temperature is around $3\epsilon_u/k_B$ for the most stable systems (oI and hP). Logically, systems with tI and tP parameters show lower melting points. An estimation of melting temperature T_{melt} and enthalpy ΔH_{melt} for all systems is given in Table II. The melting temperature is estimated by the inflection point along the enthalpy variation. The melting enthalpy is estimated by the enthalpy jump between the two enthalpy asymptotes before and after the crystal melting point. Note that the melting enthalpy is approximately the same for all systems.

C. Isothermal crystallization

1. Crystallization

In this section, we test the ability of these systems to crystallize.

Before cooling the polymer melts obtained by the RLP algorithm, the system has to be equilibrated. Figure 5 shows the mean square internal distance (MSID) [69] for the oI parameters (see Table I) after long relaxation at $T = 4\,\epsilon_u/k_B$. The MSID(n) is the average squared distance between monomers j and $j + n$ of the same chain. Note that for all the structures, the MSID stabilizes after about $10^4\tau_u$. It is worth noticing that the plateau values obtained for large n are much higher compared to the "classical soft chains" MSID published by Auhl *et al.* [69] where $\sigma = 1\sigma_u$ and $\epsilon = 1\epsilon_u$. This was an expected result as a specific σ parameter (higher than 1) leads indirectly to

TABLE I. Optimum set of parameters for all the structures after minimization.

	tP	tI	oI	hP	hcP
c (units of σ_u)	0.995	0.995	0.995	0.995	0.997
a (units of σ_u)	1.936	2.705	1.975	1.999	3.325
b (units of σ_u)	1.936	2.705	3.420	1.999	3.325
σ (units of σ_u)	1.875	1.862	1.888	1.895	1.852

TABLE II. Estimation of enthalpy ΔH_{melt} and temperature T_{melt} of melting for the four investigated systems.

	tP	tI	oI	hP
ΔH_{melt} (units of ϵ_u)	1.9	1.9	1.9	2.0
T_{melt} (units of ϵ_u/k_B)	2.9	2.9	3.1	3.1

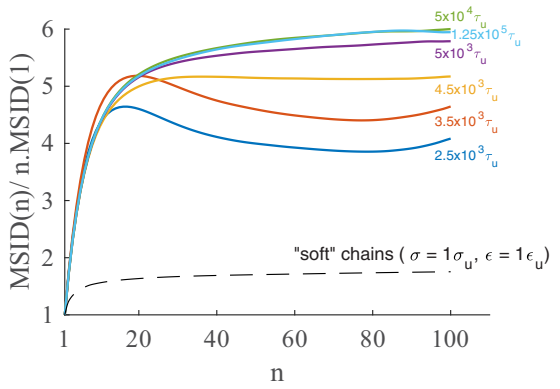

FIG. 5. Evolution and convergence over time of mean square internal distances of polymer melts for the oI parameters (see Table I). The colors blue, red, yellow, purple, green, and cyan from bottom to top, respectively, correspond to the relaxation time $2.5 \times 10^3\tau_u$, $3.5 \times 10^3\tau_u$, $4.5 \times 10^3\tau_u$, $5 \times 10^3\tau_u$, $2.5 \times 10^4\tau_u$, and $1.25 \times 10^5\tau_u$. The dashed line shows the mean square internal distances for the "classical soft chain" parameters used by Auhl *et al.* [69] for $\sigma = 1\sigma_u$ and $\epsilon = 1\epsilon_u$.

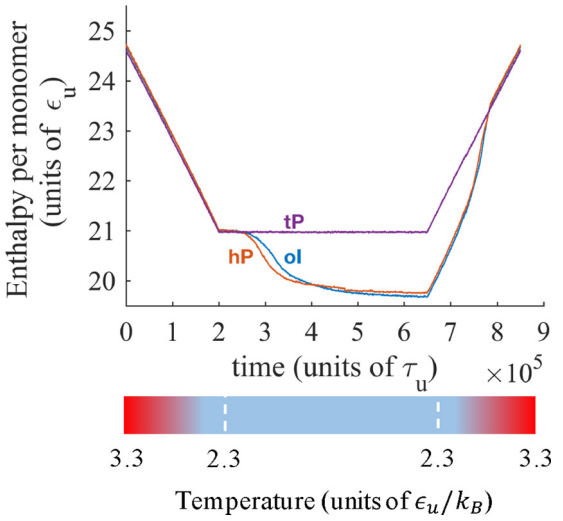

FIG. 6. Thermogram ($T = 3.3$ to $2.3\epsilon_u/k_B$, isothermal stage of $4.5 \times 10^5\tau_u$, then $T = 2.3$ to $T = 4\epsilon_u/k_B$) starting from equilibrated liquid phase for body-centered orthorhombic (oI), hexagonal primitive (hP), and simple tetragonal (tP) parameters.

stiffen the chain. Indeed, the Lennard-Jones potential has no effect on the first neighbor whereas it can be in interaction with the following neighbors. When considering three successive beads in the same chain, as σ is close to $2\sigma_u$, the third bead (second neighbor) should be at a distance of about $2\sigma_u$ from the first bead and then three beads should be aligned. It is then clear that the use of these specific values of σ favors the crystallization as found when scanning the energy landscape in a $(\sigma,\ a/c)$ space. This simple Lennard-Jones potential acts as an angular potential that helps at aligning the beads in a chain. From a computation time point of view, it is worth noticing that this method is performing as a single Lennard-Jones potential allowing both the chain alignment and interchain distance that prohibits cubic lattices.

During the cooling stage of the resulting equilibrated polymer melts from $T = 3.3$ to $2.3\epsilon_u/k_B$, the enthalpy varies linearly with time, see Fig. 6, which indicates a negligible crystallization. During the isothermal plateau at $2.3\epsilon_u/k_B$, after an incubation time of about $5 \times 10^4\tau_u$, crystallization starts and the enthalpy follows a classical sigmoidal curve for oI and hP parameters; see Fig. 6. No crystallization is observed for tP parameters. An estimation of crystallization enthalpy is given in Table III. After about $4 \times 10^5\tau_u$, the dynamics is extremely slow, probably due to (i) in the amorphous phase, the presence of both crystallite and residual entanglements that prevent the nucleation of new crystallites; (ii) existing crystals that impinge on each other. The obtained structure is then reheated until melting, which occurs at 2.9 and $2.8\epsilon_u/k_B$ for, respectively, oI and hP parameters; see Table III. Note that both systems exhibit the same behavior. In addition, the relatively high melting temperature and the significant melting enthalpy, as well as the continuous decrease of enthalpy during crystallization are strong evidence of the thermodynamic stability of the crystal phase for all studied systems.

TABLE III. Estimation of enthalpy of melting ΔH_{melt} and crystallization ΔH_{crys} and temperature of melting T_{melt} for oI, hP, and tP systems.

	oI	hP	tP
ΔH_{crys} (units of ϵ_u)	–1.1	–1.0	No
ΔH_{melt} (units of ϵ_u)	1.5	1.4	No
T_{melt} (units of ϵ_u/k_B)	2.9	2.8	No

2. *Crystallinity*

In order to quantify the crystallinity as well as the size distribution of crystallites one can use the nematic tensor and deduce an order parameter [17]. Here we have used the same physical ideas but with an algorithm based on hierarchical clustering [70] which can be employed as an optimized cluster analysis algorithm for determining phase size distribution in a matrix. This algorithm seeks to build a hierarchy of clusters and the agglomerative strategy has been used. It is a bottom-up approach: each local misorientation starts in its own cluster and several clusters are merged as one moves up the tree structure. The misorientation of the polymer chains is evaluated as follows: neighboring atoms i and j belong to the same cluster, or crystallite, if their misorientation is lower than 0.1 (approximately 5°). The misorientation between atoms i and j is defined as[2]

$$\Delta\mathbf{O}(i,j) = \min[\|\mathbf{O}(i) + \mathbf{O}(j)\|, \|\mathbf{O}(i) - \mathbf{O}(j)\|], \quad (3)$$

where $\mathbf{O}(n)$ is a unit vector giving the chain orientation at the location of the nth atom inside a chain with respect to its covalent FENE bonded neighbors:

$$\mathbf{O}(n) = \frac{\boldsymbol{r}_{n+1} - \boldsymbol{r}_{n-1}}{\|\boldsymbol{r}_{n+1} - \boldsymbol{r}_{n-1}\|}, \quad (4)$$

[2]The min operator accounts for the case where two orientation vectors are well aligned but pointing to opposite directions.

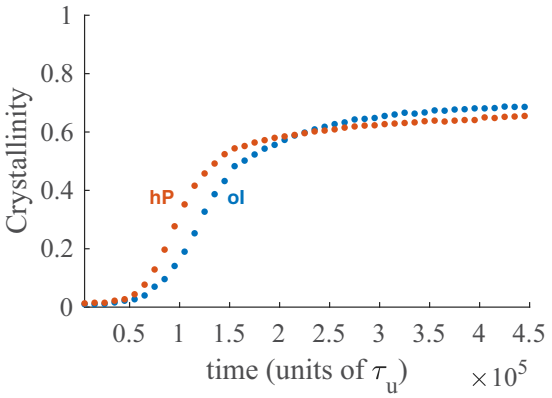

FIG. 7. Crystallinity evolution during $4.5 \times 10^5 \tau_u$ at $T = 2.3\ \epsilon_u/k_B$ for body-centered orthorhombic (oI) and hexagonal primitive (hP) parameters.

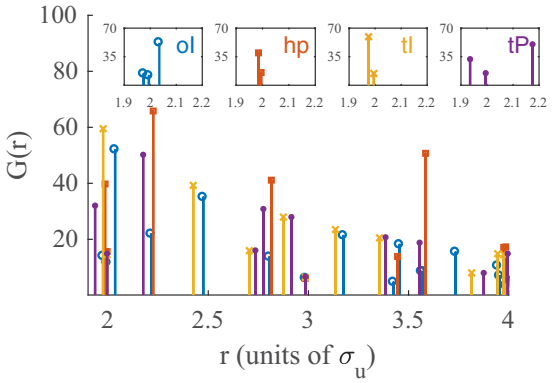

FIG. 8. Radial distribution function of perfect crystal for all optimized perfect structures (given in Table I). The colors blue, red, yellow, and purple associated with the ends of peaks' circle, square, cross, and point, respectively, correspond to the oI, hP, tI, and tP structures. In the insets, a more detailed description of RDF around $2\ \sigma_u$ for oI, hP, tI, and tP structures (corresponding to the first nearest neighbors) is given.

where $\boldsymbol{r}_n$ is the position of the nth atom inside a chain. The orientation of the chains' ends is set at the one of their first covalent FENE bonded neighbors.

The crystallinity is defined as the ratio of the number of beads belonging to a crystallite over the total number of beads. We plot the crystallinity during the isothermal plateau at $T = 2.3\epsilon_u/k_B$ in Fig. 7. At the end of the isothermal treatment, crystallinity reaches 65%. This value is comparable to the maximal crystallinity (about 80%) of real entangled polymers after long thermal treatment. However, our model crystallizes remarkably well taking into account the relative short simulation time. This is not surprising considering the optimization of the Lennard-Jones σ parameter performed before.

3. *Crystallography of crystallites*

The radial distribution function (RDF) is a powerful tool for analyzing local ordering. For the sake of comparison, we plot the RDFs of all optimized perfect structures (given in Table I) in Fig. 8. First, peaks close to multiples of FENE bond length correspond to successive intrachain neighbors, which is the signature of aligned chains (the peak at $r = 1\sigma_u$ is not shown in Fig. 8). The interchain peaks are very different for all structures, which is convenient for distinguishing them. However, the two structures, hP and oI, corresponding to the most favorable structures and to the only ones that crystallized during isothermal treatment, often present similar RDF signatures (see double peaks in the first two insets of Fig. 8). This highlights the similarity of these structures. Indeed, when moving down the central atom of the oI structure of $1/2c$, the hP structure is obtained. Nonetheless, the oI structure presents additional isolated peaks and only hP and tI structures do not show any peak between 2 and $2.2\sigma_u$ (see insets of Fig. 8).

At the end of the isothermal of the thermal treatments with optimized oI and hP σ parameters, the systems have been minimized with a conjugate gradient algorithm and the crystalline zones have been extracted with the algorithm explained before. The radial distribution functions of these crystalline zones are presented in Fig. 9 and can help us to determine the crystal structures that appear (the peak at $r = 1\sigma_u$ is not shown in Fig. 9).

The two distributions for oI and hP structure are very similar which is consistent with the thermogram as well as the energy valley presented in Fig. 3. They exhibit only a few peaks of weak intensity indicating that these structures contain defects. We observe all the intrachain distances for integer values of r and only two broad peaks at around $2.1\sigma_u$ and $3.7\sigma_u$, which are features of interchain distances. Now, focusing on these two interchain peaks, one can see in the left inset of Fig. 9 that in the range $2 - 2.2\sigma_u$ only oI and tP perfect structures present a peak and in the right inset that in the range $3.5 - 3.8\sigma_u$, tP, hP and oI are all represented. Considering the top view snapshot of the crystal zones [see Fig. 11(b)] one can clearly guess oI

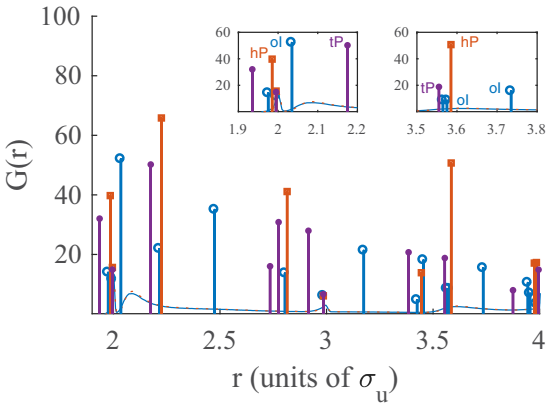

FIG. 9. Radial distribution function of crystals after quenching at $T = 2.3\epsilon_u/k_B$ and $4.5 \times 10^5 \tau_u$ for oI (blue line) and hP (dotted red line) structures. The two distributions are very similar. The vertical lines correspond to the radial distribution function of a perfect crystal for oI (in blue with circle ends), hP (in red with square ends), and tP (in purple with point ends) as shown in Fig. 8. The two distributions are very similar. In the insets, a more detailed description of the radial distribution function around $2\ \sigma_u$ is given.

or hP structure but not tP structure as no square pattern can be seen, so we can eliminate it. Note that from the inspection of Fig. 11(b) we infer values of the lattice parameters a and b are very close to the values found from the static analysis of Sec. II for the oI structure. Finally, the peak around $2.1\sigma_u$, which ensures the oI structure in crystallites, and the fact that only a few peaks appear in these radial distributions, is probably due to the fact that the observed structure is a mix of oI and hP that breaks a lot of symmetries leading to the observed result. This result likely implies that the sliding of the chains is relatively easy along the axis of the chain. Note that the same thermal treatment for tP and tI σ parameters with smaller temperature also yields crystallization. The RDFs so obtained display a behavior suggesting a mix of oI and hP crystallites. This result is reasonable as for the perfect crystal structures oI and hP, the energy per atom is nearly the same (see Fig. 3). In fact, the transition from oI into hP consists only in a shearing of half of theFENE bond distance in the chain direction which requires a very small amount of energy (evaluated to only about $0.001\epsilon_u$).

4. Crystallite shape and chain topology

Using the above-described procedure, the crystallites have been detected at different time steps at $T = 2.3\,\epsilon_u/k_B$. During the first steps, few nuclei appear and disappear, as they are unstable (see small orange regions in the first snapshot of Fig. 10). Then a very small number of nuclei reach the critical size so that they can grow (see the second snapshot of Fig. 10). At the end of the simulation for the oI parameters, only five independent crystallites have grown and the system reaches about 65% of crystallinity (see the third snapshot of Fig. 10).

The nucleus is formed after a local reorganization of a small number of chains leading to few segments aligned in the chain direction. Then we can see a relatively rapid growth in the direction perpendicular to the chain direction, whereas the growth in the chain direction is relatively limited, as depicted in Fig. 11 for the largest crystallite. This feature is consistent with what is observed experimentally for the lamellar semicrystalline organization. These results are also consistent with the previous MD simulations [20,54]. At the end of simulation, the largest crystallite is more than three times longer than thick; see Fig. 11. One can notice too that the direction of the crystallites is not correlated which implies that the amorphous phase is isotropic.

Concerning the amorphous phase, it has been checked that nearly all the chains are linked to at least one crystallite. Some chains are folded, and some are pending, loop, or tie chains as one can see in Fig. 12. For example, in the largest crystal, we count 1386 loops, 264 folding, 1583 pending, and 850 tie chains for 3814 pieces of chain in the crystal. These chain topologies are similar to the ones found in real semicrystalline polymers. For perspective, we will study the statistics for all these topologies for different time-temperature protocols.

Additional isothermal crystallization tests have been performed at lower temperatures $(2.2; 2.1; 2.0\epsilon_u/k_B)$. As expected, the size distribution of the crystallites is shifted towards lower values as the temperature is lower, but the crystallinity remains nearly constant. These results are also compatible with

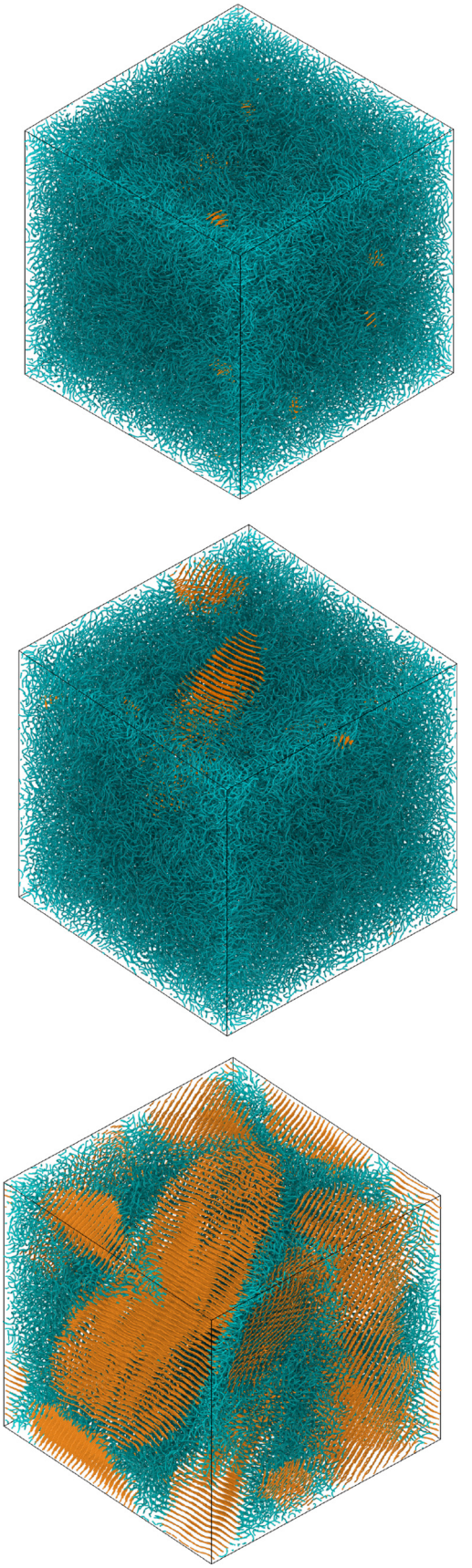

FIG. 10. Crystal nucleation and growth for the oI system during the isothermal treatment at $T = 2.3\epsilon_u/k_B$ (from top to bottom). In blue is the amorphous phase, and in orange the crystal phase.

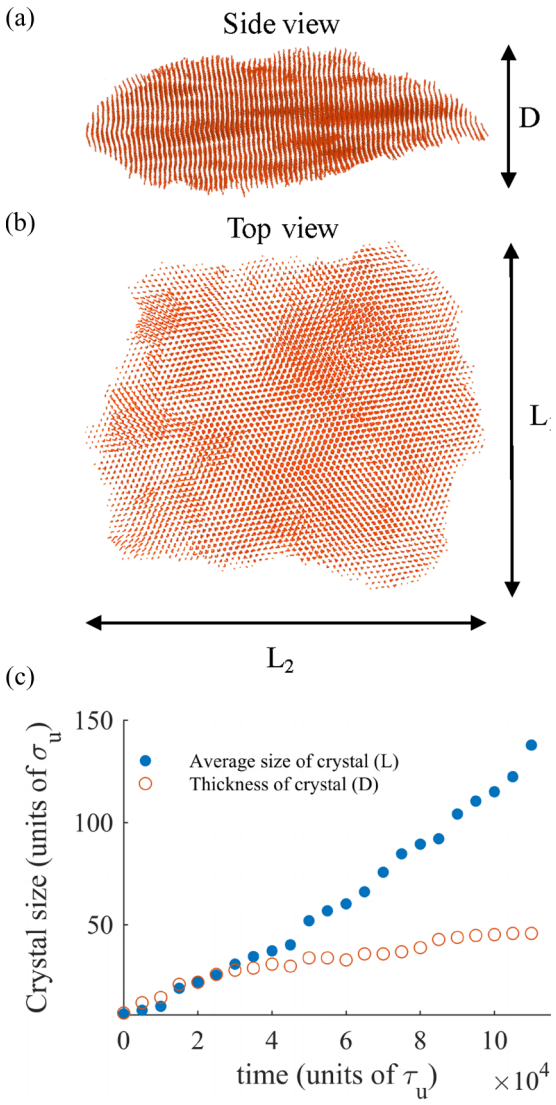

FIG. 11. (a) Side and (b) top view of the largest crystal with oI parameters. (c) Size of the same crystal; D the thickness and $L = (L_1 + L_2)/2$ the average width, during its growth.

thermodynamic considerations. At $T = 2.0\,\epsilon_u/k_B$ the lamellar structure is essentially lost which would correspond for a real polymer to a strong quench.

IV. CONCLUSION

In this paper, we have used a simple coarse-grained model to analyze the microstructural properties of semicrystalline polymers. In this model, the monomer bonds inside the chains are described by a FENE potential, whereas the pair interactions are described by a Lennard-Jones potential without any angular potential term. By modifying the σ value of the Lennard-Jones potential, and using an energetic analysis, it has been possible to show that two different structures, hexagonal primitive (hP) and body-centered orthorhombic (oI) show nearly the same stability. These structures need a σ parameter close to $2\,\sigma_u$ which tends to align three successive beads in a chain, mimicking the angular potential. It is worth noticing that every σ parameter used for a given

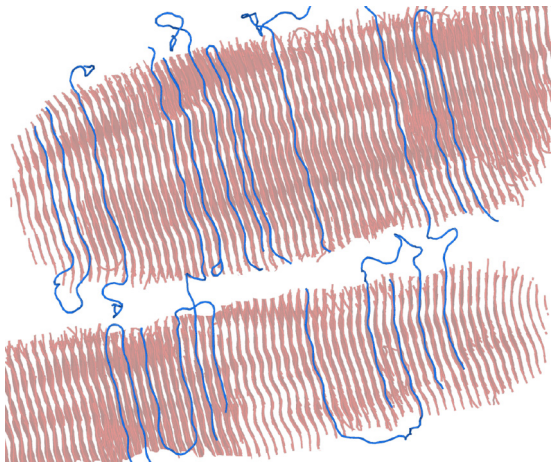

FIG. 12. Cross section of two close crystals with some examples of classical type of chains detected in semicrystal: folded, loop, tie and cilia (in blue). Here only the amorphous phase of classical type of selected chains is shown to facilitate reading of the figure. This structure was obtained at $T = 2.3\,\epsilon_u/k_B$ after $4.5 \times 10^5 \tau_u$.

FENE Lennard-Jones system induces an equivalent angular potential corresponding to a more folded chain. As an example, when using $\sigma = 1\sigma_u$ the local equilibrium for three successive beads in a chain is obtained for an equilateral triangle. Our model does not allow cubic symmetry, as the Lennard-Jones equilibrium distance is significantly different from the distance between two successive beads in a chain. This is realistic from the physical point of view as the distance between two chains is always significantly different from the distance between two monomers in the same chain for the real polymers. The two obtained structures (oI and hP) are similar and the system can evolve from one to the other by a slight shearing in the chain direction.

Starting with an equilibrated polymer liquid, we have shown that lamellar crystallites can be obtained quickly when choosing an optimized crystallization temperature. In this condition, these systems remarkably mimic the chain topology in semicrystalline polymers. Indeed, folded chains and loop chains as well as tie chains have been formed during the crystallization. The crystallinity of about 60%–70% is also compatible with typical semicrystalline polymers (e.g., polyolefin, polyamides, polyesters, etc.). In conclusion, using a simple model with only Lennard-Jones and FENE potential, it has been possible to reproduce the six points mentioned in the Introduction that are required to mimic satisfactorily a semicrystalline microstructure. It is a tool that is adapted to analyze the crystallization phenomenon and to study the general features of semicrystalline microstructures like the topology of amorphous chains, e.g., the probability to form a tie chain or a loop chain.

ACKNOWLEDGMENTS

The authors thank Professor Jean-Louis Barrat for useful discussions. This work was performed using HPC resources from the FLMSN, "Fédération Lyonnaise de Modélisation et Sciences Numériques," partner of EQUIPEX EQUIP@MESO.

[1] P. B. Bowden and R. J. Young, J. Mater. Sci. **9**, 2034 (1974).
[2] J. M. Haudin, *Plastic Deformation of Amorphous and Semicrystalline Materials* (Editions de Physique, Paris, 1982).
[3] A. Galeski, Prog. Polym. Sci. **28**, 1643 (2003).
[4] E. F. Oleinik, Polym. Sci., Ser. C **45**, 17 (2003).
[5] S. Patlazhan and Y. Remond, J. Mater. Sci. **47**, 6749 (2012).
[6] B. Xiong, O. Lame, J.-M. Chenal, C. Rochas, R. Seguela, and G. Vigier, Macromolecules **48**, 5267 (2015).
[7] R. Seguela, J. Polym. Sci., Part B: Polym. Phys. **43**, 1729 (2005).
[8] N. Brown and I. M. Ward, J. Mater. Sci. **18**, 1405 (1983).
[9] J. T. Yeh and J. Runt, J. Polym. Sci., Part B: Polym. Phys. **29**, 371 (1991).
[10] Z. Bartczak, Macromolecules **38**, 7702 (2005).
[11] R. Séguéla, Macromol. Mater. Eng. **292**, 235 (2007).
[12] J.-L. Barrat, J. Baschnagel, and A. Lyulin, Soft Matter **6**, 3430 (2010).
[13] A. Makke, M. Perez, O. Lame, and J.-L. Barrat, J. Chem. Phys. **131**, 014904 (2009).
[14] A. Makke, M. Perez, O. Lame, and J.-L. Barrat, Proc. Natl. Acad. Sci. USA **109**, 680 (2012).
[15] A. Makke, O. Lame, M. Perez, and J.-L. Barrat, Macromolecules **45**, 8445 (2012).
[16] S. Jabbari-Farouji, J. Rottler, O. Lame, A. Makke, M. Perez, and J.-L. Barrat, J. Phys.: Condens. Matter **27**, 194131 (2015).
[17] S. Jabbari-Farouji, J. Rottler, O. Lame, A. Makke, M. Perez, and J.-L. Barrat, ACS Macro Lett. **4**, 147 (2015).
[18] B. Monasse, S. Queyroy, and O. Lhost, Int. J. Mater. Form. **1**, 1111 (2008).
[19] S. Queyroy and B. Monasse, J. Appl. Polym. Sci. **125**, 4358 (2012).
[20] T. Yamamoto, Polymer **50**, 1975 (2009).
[21] S. Fujiwara and T. Sato, J. Chem. Phys. **107**, 613 (1997).
[22] T. A. Kavassalis and P. R. Sundararajan, Macromolecules **26**, 4144 (1993).
[23] P. R. Sundararajan and T. A. Kavassalis, J. Chem. Soc. Faraday Trans. **91**, 2541 (1995).
[24] C. Liu and M. Muthukumar, J. Chem. Phys. **109**, 2536 (1998).
[25] M. Muthukumar and P. Welch, Polymer **41**, 8833 (2000).
[26] P. Welch and M. Muthukumar, Phys. Rev. Lett. **87**, 218302 (2001).
[27] I. Dukovski and M. Muthukumar, J. Chem. Phys. **118**, 6648 (2003).
[28] H. Takeuchi, J. Chem. Phys. **109**, 5614 (1998).
[29] S. Fujiwara and T. Sato, Phys. Rev. Lett. **80**, 991 (1998).
[30] T. Shimizu and T. Yamamoto, J. Chem. Phys. **113**, 3351 (2000).
[31] R. H. Gee, N. Lacevic, and L. E. Fried, Nat. Mater. **5**, 39 (2006).
[32] T. Yamamoto, J. Chem. Phys. **129**, 184903 (2008).
[33] P. Yi, C. R. Locker, and G. C. Rutledge, Macromolecules **46**, 4723 (2013).
[34] T. Yamamoto, J. Chem. Phys. **109**, 4638 (1998).
[35] N. Waheed, M. S. Lavine, and G. C. Rutledge, J. Chem. Phys. **116**, 2301 (2002).
[36] N. Waheed, M. J. Ko, and G. C. Rutledge, Polymer **46**, 8689 (2005).
[37] T. Yamamoto, J. Chem. Phys. **139**, 054903 (2013).
[38] T. Yamamoto, J. Chem. Phys. **115**, 8675 (2001).
[39] T. Yamamoto, Polymer **45**, 1357 (2004).
[40] M. S. Lavine, N. Waheed, and G. C. Rutledge, Polymer **44**, 1771 (2003).
[41] M. J. Ko, N. Waheed, M. S. Lavine, and G. C. Rutledge, J. Chem. Phys. **121**, 2823 (2004).
[42] A. Koyama, T. Yamamoto, K. Fukao, and Y. Miyamoto, Phys. Rev. E **65**, 050801 (2002).
[43] T. Yamamoto, J. Macromol. Sci., Part B: Phys. **42**, 629 (2003).
[44] T. Yamamoto, Polymer **54**, 3086 (2013).
[45] T. Yamamoto, Macromolecules **47**, 3192 (2014).
[46] T. Yamamoto, J. Chem. Phys. **133**, 034904 (2010).
[47] T. Yamamoto, in *Interphases and Mesophases in Polymer Crystalliztion III*, edited by G. Allegra (Springer-Verlag, Berlin/Heidelberg, 2005), pp. 37–85.
[48] K. Kremer and G. S. Grest, J. Chem. Phys. **92**, 5057 (1990).
[49] C. F. Abrams and K. Kremer, J. Chem. Phys. **115**, 2776 (2001).
[50] R. Everaers and K. Kremer, in *Anomalous Diffusion from Basics to Applications*, Proceedings of the XIth Max Born Symposium, Ladek-Zdrój, Poland, 1998, edited by A. Pekalski and K. Sznajd-Weron (Springer, Berlin, 1999), pp. 221–234.
[51] D. Reith, H. Meyer, and F. Müller-Plathe, Macromolecules **34**, 2335 (2001).
[52] H. Meyer and F. Müller-Plathe, J. Chem. Phys. **115**, 7807 (2001).
[53] H. Meyer and F. Müller-Plathe, Macromolecules **35**, 1241 (2002).
[54] C. Luo and J.-U. Sommer, Macromolecules **44**, 1523 (2011).
[55] C. Luo and J.-U. Sommer, Phys. Rev. Lett. **112**, 195702 (2014).
[56] C. Luo, M. Kröger, and J.-U. Sommer, Polymer **109**, 71 (2017).
[57] R. S. Hoy and N. C. Karayiannis, Phys. Rev. E **88**, 012601 (2013).
[58] H. T. Nguyen, T. B. Smith, R. S. Hoy, and N. C. Karayiannis, J. Chem. Phys. **143**, 144901 (2015).
[59] T. Vettorel and H. Meyer, J. Chem. Theory Comput. **2**, 616 (2006).
[60] T. Vettorel, H. Meyer, J. Baschnagel, and M. Fuchs, Phys. Rev. E **75**, 041801 (2007).
[61] S. Lee and G. C. Rutledge, Macromolecules **44**, 3096 (2011).
[62] J. Che, C. R. Locker, S. Lee, G. C. Rutledge, B. S. Hsiao, and A. H. Tsou, Macromolecules **46**, 5279 (2013).
[63] J. M. Kim, R. Locker, and G. C. Rutledge, Macromolecules **47**, 2515 (2014).
[64] I.-C. Yeh, J. W. Andzelm, and G. C. Rutledge, Macromolecules **48**, 4228 (2015).
[65] J. Rottler, J. Phys.: Condens. Matter **21**, 463101 (2009).
[66] R. S. Hoy and M. O. Robbins, J. Polym. Sci., Part B: Polym. Phys. **44**, 3487 (2006).
[67] M. Perez, O. Lame, F. Leonforte, and J.-L. Barrat, J. Chem. Phys. **128**, 234904 (2008).
[68] G. Subramanian, J. Chem. Phys. **133**, 164902 (2010).
[69] R. Auhl, R. Everaers, G. S. Grest, K. Kremer, and S. J. Plimpton, J. Chem. Phys. **119**, 12718 (2003).
[70] L. Rokach and O. Maimon, in *Data Mining and Knowledge Discovery Handbook*, edited by O. Maimon and L. Rokach (Springer US, Boston, MA, 2005), pp. 321–352.